Computer Assisted Mechanics and Engineering Sciences, 10: 1–22, 2003.

A coupled three-phase FE-model for dewatering of soils by means of compressed air

Gerhard Oettl, Rudolf F. Stark, Guenter Hofstetter
University of Innsbruck, Department of Civil Engineering
Institute for Structural Analysis and Strength of Materials
A-6020 Innsbruck, Austria

(Received November 3, 2000)

A coupled three-phase soil model, consisting of a deformable soil skeleton and the fluid phases water and compressed air, applicable for tunnelling below the ground-water table by means of compressed air, is presented. In this model interactions of the flow of the fluids in the soil with the deformations of the soil skeleton are taken into account in a physically consistent manner. The theoretical background and the implementation of the model into a finite element code are briefly addressed. Several applications dealing with the numerical simulation of laboratory tests and a full-scale in-situ experiment are discussed. These experiments focus on the flow of (compressed) air in dry as well as semi-saturated soil.

1. Introduction

The construction of shallow tunnels, located below the ground-water level, is an important topic in geotechnical engineering. In this case deformations of the ground and surface settlements are not only caused by the advance of the tunnel face but also by dewatering of the soil. Especially in urban areas the minimization of surface settlements during the construction of the tunnel plays a predominant role in order to avoid damage of existing buildings and infrastructure. For tunnels driven in aquifers displacement of the ground-water from the working area at the tunnel face is essential. Compared to lowering the ground-water table with pumping wells and driving the tunnel under atmospheric conditions, the application of compressed air for displacing the ground-water yields smaller settlements as shown in a study conducted during the subway construction in Essen, Germany [12]. This advantage is due to the drag forces of the airflow in the soil which counteract the deformations caused by dewatering and tunnel excavation

The research project addressed in this paper is part of the *Austrian Joint Research Initiative* on *Numerical Simulation in Tunnelling*. It deals with the development and application of a three-dimensional numerical model for tunnelling below the ground-water table taking into account compressed air as a means for dewatering the soil in the vicinity of the tunnel face. The principle sketch in Fig. 1 shows the loss of compressed air at the tunnel face and through cracks in the shotcrete lining as well as the flow of compressed air in the adjacent soil.

Basically, there exist two different solution strategies for the numerical simulation of tunnelling under compressed air. In the uncoupled approach the flow of water and compressed air in the soil and the deformations of the soil caused by dewatering as well as by the advance of the tunnel face are treated in two consecutive steps. Consequently, interactions between the fluid flow through the pores and the deformations of the soil skeleton are neglected. On the other hand, the coupled solution procedure adopted in this study permits consideration of the intrinsic coupling of the process of dewatering with the deformations of the soil. Only the latter approach allows to properly take into account interactions of the flow of water and compressed air in the soil with the deformations of the soil skeleton in a physically consistent manner.

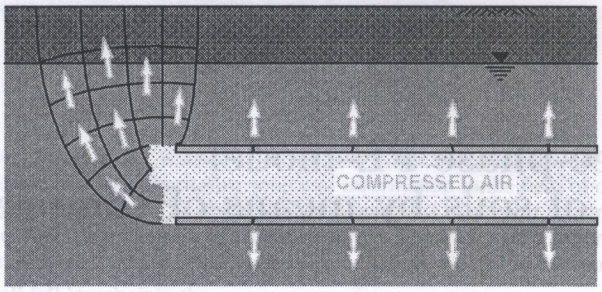

Fig. 1. Tunnelling under compressed air

The paper is organized as follows: First of all the governing equations of the three-phase soil model are presented based on respective mathematical models available in the literature [14, 17], followed by the weak formulation of the governing equations and by the discretization within the framework of the finite element method. The second part of this paper is devoted to the validation and application of the model. Two examples refer to the numerical simulation of laboratory tests dealing with the flow of compressed air through dry soil and with dewatering of soil by gravity. The third example contains the numerical simulation of a large-scale in-situ test for dewatering by means of compressed air, carried out at Essen [12].

2. Governing equations for a three-phase formulation

The coupled numerical model for dewatering by means of compressed air relies on a soil model treating the soil as a three-phase medium consisting of the deformable soil skeleton and the two fluid phases water and compressed air. Generally there exist various approaches for the mathematical description of multi-phase media: (i) Mixture theory starts from the macroscopic level and can be viewed as an extension of the classical continuum mechanics theory. Employing the concept of volume fractions allows to account for the different constituents of the soil; (ii) applying the balance laws of classical continuum mechanics to the actual microstructure of the porous medium and using so-called averaging operators to arrive at the macroscopic level (i.e. employing averaging theory) yields the same governing equations for the multi-phase medium as shown in [3]; (iii) alternatively, the basic equations can also be derived by extending Biot's theory [2] as outlined, e.g., in [14, 18].

The mathematical description of the three-phase medium pursued in the present paper follows [14, 17]. At the outset averaged quantities for the density of the three-phase mixture, for the stresses acting on the surfaces of a differential volume element of the mixture and for the velocities of the individual fluid phases relative to the soil skeleton are defined. Following this elementary definitions the governing equations for the three-phase formulation, which consist of the kinematic relations, the equilibrium equations for the three-phase mixture, the mass balance equations, the constitutive equations for each phase and of a constitutive relationship between the capillary stress and the degree of water saturation, are discussed briefly.

2.1. Definition of averaged quantities for the three-phase medium

A soil element can be thought of as a mixture of the three phases soil grains, water and compressed air which continuously fill the entire volume according to their percentile share. Of paramount importance for deriving the governing equations of the model is the definition of averaged values for the density, the stresses and the fluid velocities relative to the soil skeleton. Figure 2 shows a section of a representative elementary volume (REV) of the soil (a) before and (b) after averaging.

The three constituents solid phase s, water w and compressed air a occupy the parts $\mathrm{d}V^s$, $\mathrm{d}V^w$ and $\mathrm{d}V^a$ of the volume $\mathrm{d}V$ of the REV. Introducing the porosity n of the soil, defined as the ratio of the pore volume to the total volume of the REV, and the degree of saturation of the respective

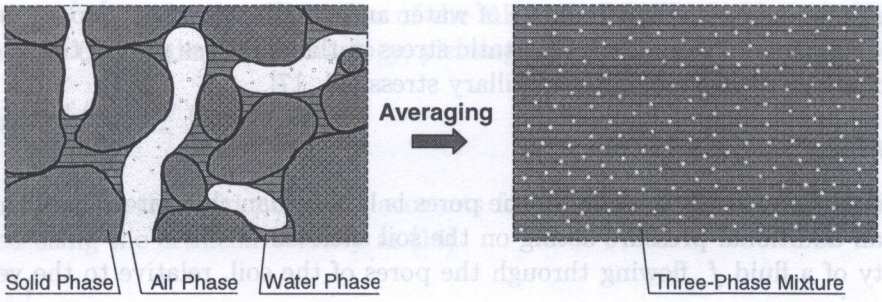

Fig. 2. Averaging of the three-phase medium

fluid phase S^f $(f = w, a)$, indicating the part of the void space filled by the particular fluid, yields the following definitions for the volume fractions:

$$\frac{\mathrm{d}V^s}{\mathrm{d}V} = (1-n), \qquad \frac{\mathrm{d}V^w}{\mathrm{d}V} = nS^w, \qquad \frac{\mathrm{d}V^a}{\mathrm{d}V} = nS^a. \tag{1}$$

For the degrees of saturation the condition $S^w + S^a = 1$ holds. The partial surface elements of the individual constituents, $\mathrm{d}A^s$, $\mathrm{d}A^w$ and $\mathrm{d}A^a$, are assumed to be related to the surface element $\mathrm{d}A$ of the three-phase mixture in the same way as the respective partial volumes of the different phases to the volume of the REV.

Assuming each constituent to fill the entire volume $\mathrm{d}V$ of the soil element according to its volume fraction (1) yields the averaged density of the three-phase mixture

$$\tilde{\rho} = (1-n)\rho^s + nS^w\rho^w + nS^a\rho^a\,, \tag{2}$$

ρ^s, ρ^w and ρ^a being the intrinsic densities of the three phases.

Using the ratios for the partial surface elements of the individual constituents the stress tensor for the three-phase material can be defined as

$$\tilde{\boldsymbol{\sigma}} = (1-n)\boldsymbol{\sigma}^s + nS^w\boldsymbol{\sigma}^w + nS^a\boldsymbol{\sigma}^a\,, \tag{3}$$

$\boldsymbol{\sigma}^s$, $\boldsymbol{\sigma}^w$ and $\boldsymbol{\sigma}^a$ being the respective stress tensors of the individual phases. Since the stress state in the fluid phases is considered as a hydrostatic one, $\boldsymbol{\sigma}^w = p^w\,\mathbf{1}$ and $\boldsymbol{\sigma}^a = p^a\,\mathbf{1}$ can be used to rewrite Eq. (3) as

$$\tilde{\boldsymbol{\sigma}} = (1-n)\boldsymbol{\sigma}^s + n(S^w p^w + S^a p^a)\,\mathbf{1}\,, \tag{4}$$

where $\mathbf{1}$ denotes the second-order unit tensor and p^w and p^a are the hydrostatic stresses in the two fluid phases. Using the effective stress tensor

$$\tilde{\boldsymbol{\sigma}}' = (1-n)\left[\boldsymbol{\sigma}^s - (S^w p^w + S^a p^a)\,\mathbf{1}\right], \tag{5}$$

Eq. (4) can be reformulated as

$$\tilde{\boldsymbol{\sigma}} = \tilde{\boldsymbol{\sigma}}' + (S^w p^w + S^a p^a)\,\mathbf{1}\,. \tag{6}$$

For both the soil skeleton and the fluid phases tensile stresses are defined as positive quantities. The total averaged stress tensor is partitioned into the effective stresses and the fluid stresses. Due to the assumption of incompressible soil grains only the former cause deformations of the soil skeleton. Thus, the constitutive law for the soil skeleton will be formulated in terms of effective stresses.

In the context of dewatering by means of compressed air it seems to be reasonable to assume isothermal conditions and to consider the water in the pores of the soil being present as condensed

liquid, i.e. the pores only contain a mixture of water and air. Hence, water vapour is not taken into account. The difference between the hydrostatic stress in the air phase p^a and the hydrostatic stress in the water phase p^w is defined as the capillary stress [14, 17],

$$p^c = p^a - p^w \,. \tag{7}$$

Due to surface tension the air pressure in the pores is larger than the water pressure. Hence, p^c can be viewed as an additional pressure acting on the soil skeleton.

The velocity of a fluid f, flowing through the pores of the soil, relative to the velocity $\mathbf{v}$ of the soil skeleton is given as

$$\mathbf{v}^{fr} = \mathbf{v}^f - \mathbf{v} \,, \tag{8}$$

where $\mathbf{v}^f$ is the intrinsic velocity of the fluid. Since the flow of the fluid phase f occurs through the partial surface $\mathrm{d}A^f$ of $\mathrm{d}A$, the relative velocity averaged over $\mathrm{d}A$, the so-called artificial velocity, is obtained as

$$\tilde{\mathbf{v}}^{fr} = nS^f \mathbf{v}^{fr} \,. \tag{9}$$

2.2. Kinematic equations

For tunnelling under compressed air the assumption of small displacements and small strains seems to be justified. Hence, the relationship between the displacements u_i , $i = 1, 2, 3$, of the soil skeleton and the strains ε_{ij} in the soil skeleton is given as

$$\varepsilon_{ij} = \frac{1}{2}\left(\frac{\partial u_i}{\partial x_j} + \frac{\partial u_j}{\partial x_i}\right) \,. \tag{10}$$

2.3. Equilibrium equations

The linear momentum balance equations for the soil skeleton are given as

$$\mathrm{d}\mathbf{R} = \frac{\mathrm{D}}{\mathrm{D}t}(\mathrm{d}m^s \, \mathbf{v}) \,, \tag{11}$$

where $\mathrm{d}m^s = (1-n)\rho^s \, \mathrm{d}V$, $\mathrm{D}/\mathrm{D}t$ denotes the material time derivative and $\mathbf{v}$ is the velocity of the soil skeleton. With $\mathrm{d}\mathbf{R}$ containing the external forces acting on the volume element under consideration and integrating over the volume and the surface of the REV, respectively, yields

$$\int_V \tilde{b}_i^s \, \mathrm{d}V + \int_S \tilde{t}_i^s \, \mathrm{d}S + \int_V f_i^s \, \mathrm{d}V = \int_V \frac{\mathrm{D}}{\mathrm{D}t}[(1-n)\rho^s \, v_i] \, \mathrm{d}V \,, \tag{12}$$

where $\tilde{b}_i^s$, $\tilde{t}_i^s$ and f_i^s denote the respective components of the body forces, the surface tractions and the interaction forces for the solid phase. Using the expressions $\tilde{b}_i^s = (1-n)\rho^s g_i$ and $\tilde{t}_i^s = (1-n)\, \sigma_{ji}^s \, n_j$ as well as the divergence theorem to transform the surface integral into a volume integral, Eq. (12) can be rewritten as

$$\int_V (1-n)\rho^s g_i \, \mathrm{d}V + \int_V (1-n)\, \sigma_{ji,j}^s \, \mathrm{d}V + \int_V f_i^s \, \mathrm{d}V = \int_V (1-n)\rho^s a_i \, \mathrm{d}V \,. \tag{13}$$

Since $\mathrm{d}m^s$ on the right hand side of Eq. (11) is constant, the material time derivative only has to be applied to the velocity $\mathbf{v}$ with a_i denoting the resulting acceleration of the soil skeleton. Finally, Eq. (13) can be formulated as [14, 17]

$$(1-n)\, \sigma_{ji,j}^s + (1-n)\rho^s (g_i - a_i) + f_i^s = 0 \,. \tag{14}$$

Using $\mathrm{d}m^f = nS^f\rho^f\,\mathrm{d}V$ for the fluid mass of the REV the linear momentum balance equation for the fluid phase f can be derived by analogy, yielding

$$nS^f\sigma^f_{ji,j} + nS^f\rho^f\left(g_i - a^f_i\right) + f^f_i = 0\,. \tag{15}$$

The interaction force for the fluid phase f^f_i accounts for viscous effects due to the fluid flow and can be expressed using the artificial velocity as [14]

$$f^f_i = -nS^f\frac{\gamma^f}{k^f}\tilde{v}^{fr}_i\,, \tag{16}$$

where k^f denotes the permeability of the soil with respect to the particular fluid phase f and γ^f is its unit weight. Inserting Eq. (16) into (15), making use of $\sigma^f_{ij} = p^f\delta_{ij}$ for the hydrostatic stress state in the fluid phase and neglecting the acceleration term, i.e. assuming quasi-static conditions, Darcy's law for the artificial velocity of a fluid relative to the soil skeleton can be derived as

$$\tilde{v}^{fr}_i = \frac{k^f}{\gamma^f}\left(p^f_{,i} + \rho^f g_i\right)\,. \tag{17}$$

For a soil fully saturated with one fluid phase (either water or air) the coefficient of permeability k^f can be considered as a constant. If two fluid phases are present in the pores k^f depends on the degree of saturation S^f such that k^f decreases with decreasing S^f. This is primarily due to the fact that water and air are assumed to be immiscible and each fluid can only flow in the part of the pores filled by the respective phase. Hence, if the degree of saturation S^f of phase f decreases, also the part of the area for the particular fluid flow is reduced, thus diminishing the permeability of the soil with respect to the fluid phase f. Defining relative permeability coefficients k^{rw} and k^{ra}, the permeabilities k^w and k^a of the soil skeleton with respect to the water and air phase can be formulated as functions of the degree of water saturation,

$$k^w(S^w) = k^{ow}\,k^{rw}(S^w)\,, \qquad k^a(S^w) = k^{oa}\,k^{ra}(S^w)\,. \tag{18}$$

In Eqs. (18) k^{ow} and k^{oa} are the permeabilities for the fully saturated states, i.e. k^{ow} refers to fully water saturated conditions ($S^w = 1$) and k^{oa} to a dry soil ($S^w = 0$), respectively. k^{rw} and k^{ra} are introduced in order to consider partially saturated states. They are scalar quantities, varying between zero and one, depending on the degree of water saturation S^w. Empirical relations $k^{rw}(S^w)$ and $k^{ra}(S^w)$ can be found in the literature [5, 6, 16]. Figure 3 shows graphs of the two curves for a typical soil.

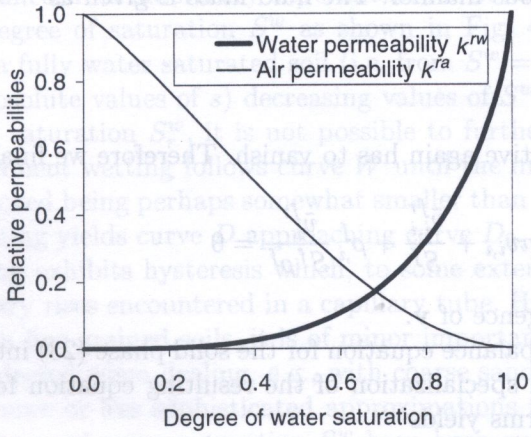

Fig. 3. Relative permeability curves

The linear momentum balance equations for the three-phase mixture are obtained by adding up Eqs. (14) and (15), the latter for both the water and the air phase,

$$(1-n)\,\sigma^s_{ji,j} + nS^w\sigma^w_{ji,j} + nS^a\sigma^a_{ji,j} + [(1-n)\rho^s + nS^w\rho^w + nS^a\rho^a]\,g_i = (1-n)\rho^s a_i + nS^w\rho^w a^w_i + nS^a\rho^a a^a_i\,. \tag{19}$$

In Eq. (19) use of the fact has been made that the interaction forces must vanish by summation of the three phases, i.e. $f^s_i + f^w_i + f^a_i = 0$. For tunnelling under compressed air, the air pressure in the tunnel is increased slowly up to the desired value. Hence, the flow of water and air as well as the pressure in the soil develop rather slowly and it is justified to assume quasi-static conditions. Consequently, Eq. (19) can be rewritten as

$$\tilde{\sigma}_{ji,j} + \tilde{\rho} g_i = 0\,, \tag{20}$$

using the averaged quantities for the density (2) and the stresses (3) of the three-phase mixture.

2.4. Mass balance equations

In each configuration the total mass of the solid phase, given as

$$m^s = \int_V (1-n)\rho^s \,\mathrm{d}V\,, \tag{21}$$

is constant; hence, $\mathrm{D}m^s/\mathrm{D}t = 0$ holds, yielding

$$\frac{\mathrm{D}m^s}{\mathrm{D}t} = \int_V \left\{ \frac{\mathrm{D}[(1-n)\rho^s]}{\mathrm{D}t} + (1-n)\rho^s \,\mathrm{div}\,\mathbf{v} \right\} \mathrm{d}V = 0\,, \tag{22}$$

$\mathbf{v}$ being the intrinsic velocity of the soil skeleton [14]. To satisfy Eq. (22) the integrand must vanish. Performing the material time derivative, taking into account the incompressibility of the solid phase (be careful in distinguishing between the solid phase and the soil skeleton, the latter is of course assumed deformable!) and using the volumetric strain rate of the soil skeleton $\dot{\varepsilon}_{vol}$ ($\dot{\varepsilon}_{vol} = \dot{\varepsilon}_{ij}\,\delta_{ij}$) instead of the divergence of $\mathbf{v}$, Eq. (22) can be rewritten as

$$\frac{\mathrm{D}n}{\mathrm{D}t} = (1-n)\,\dot{\varepsilon}_{vol}\,. \tag{23}$$

Considering a domain without any wells or sinks the mass balance equation for a fluid phase f can be derived in an analogous manner. The fluid mass is given as

$$m^f = \int_V nS^f\rho^f \,\mathrm{d}V \tag{24}$$

and its material time derivative again has to vanish. Therefore we finally get [14, 17]

$$\frac{\mathrm{D}n}{\mathrm{D}t} + \frac{n}{S^f\rho^f}\frac{\mathrm{D}(S^f\rho^f)}{\mathrm{D}t} + nv_{i,i} + \frac{\tilde{v}^{fr}_{i,i}}{S^f} + \rho^f_{,i}\frac{\tilde{v}^{fr}_i}{S^f\rho^f} = 0 \tag{25}$$

with $v_{i,i}$ denoting the divergence of $\mathbf{v}$.

Substitution of the mass balance equation for the solid phase (23) into the mass balance equation for the fluid phase (25) and specialization of the resulting equation for quasi-static conditions by neglecting the convective terms yields

$$\rho^f S^f \dot{\varepsilon}_{vol} + nS^f\dot{\rho}^f + n\rho^f\dot{S}^f = -\rho^f \,\mathrm{div}\,\tilde{\mathbf{v}}^{fr}\,. \tag{26}$$

Due to the assumption that each phase continuously fills the entire domain, the mass balance equations for the individual constituents are referred to the same volume element. Hence, Eq. (26) can be interpreted as follows: The term on the right hand side represents the inflow of fluid mass into a given control volume which has to be balanced by the terms on the left hand side of this equation; i.e. the inflow can be stored in the volume element either by an increase of the volumetric strain of the soil skeleton $\dot{\varepsilon}_{vol}$ (being associated with an increase of porosity n as in Eq. (23)), by an increase of the density $\dot{\rho}^f$ or by an increase of the degree of saturation $\dot{S}^f$ of the respective fluid phase.

2.5. Constitutive equations for the different phases

Since the solid phase is assumed to be incompressible, only the effective stresses cause deformations of the soil skeleton (note that for compressible soil grains the volumetric strains due to the hydrostatic stresses in the fluid phases would have to be taken into account, too). In soil mechanics the individual soil grains, i.e. the solid phase, are commonly assumed to be incompressible. Hence, the deformations of the soil skeleton result from relative movements of the grains within the soil skeleton. However, for other kinds of problems a compressible solid phase may be taken into account as suggested in [14]. Therefore, the non-linear constitutive law for the soil skeleton is formulated relating the rate of the averaged effective stresses to the strain rate in the soil skeleton:

$$\overset{\circ}{\tilde{\boldsymbol{\sigma}}}' = \mathbf{C}_T \, \dot{\boldsymbol{\varepsilon}} \, . \tag{27}$$

In Eq. (27) $\mathbf{C}_T = \mathrm{d}\tilde{\boldsymbol{\sigma}}'/\mathrm{d}\boldsymbol{\varepsilon}$ denotes the tangent material matrix of the soil skeleton.

The constitutive equation for a compressible barotropic fluid phase (i.e. the state of thermodynamic equilibrium is independent of the temperature) is given as

$$\frac{\dot{\rho}^f}{\rho^f} = -\frac{\dot{p}^f}{K^f} \tag{28}$$

with K^f denoting the bulk modulus of the respective fluid phase f. The minus sign on the right hand side of Eq. (28) is a consequence of having defined tensile stresses as positive quantities.

Finally, a constitutive relationship between the capillary stress p^c and the degree of water saturation S^w is required:

$$S^w = S^w(p^c) \, . \tag{29}$$

Inherent in the above equation is the assumption of isothermal conditions. Otherwise, the degree of water saturation would not only be a function of the capillary stress but also of the temperature. Equation (29) usually is obtained from laboratory experiments for determining the relation between matrix suction s and the degree of saturation S^w as shown in Fig. 4a [5]. Following curve D_0, departing from the state of a fully water saturated soil (i.e. from $S^w = 1$ and $s = 0$) for decreasing values of s (i.e. increasing absolute values of s) decreasing values of S^w are obtained. Approaching the residual degree of water saturation S_r^w, it is not possible to further withdraw water from the pores by decreasing s. Subsequent wetting follows curve W until the maximum value of the degree of water saturation S_s^w is reached being perhaps somewhat smaller than 1 because of the inclusion of air bubbles. Repeated dewetting yields curve D approaching curve D_0. As can be seen from Fig. 4a dewetting followed by wetting exhibits hysteresis which, to some extent, can be viewed similar to the active and passive capillary rises encountered in a capillary tube. However, while this hysteresis effect is rather pronounced in fine-grained soils, it is of minor importance for more coarse-textured ones and it may even be neglected when dealing, e.g., with coarse sands or gravel [7].

In the literature several more or less sophisticated approximations for the relationship between matrix suction s and the degree of water saturation S^w have been suggested. A relatively simple empirical equation was developed by Brooks and Corey (Fig. 4b) which is described in more detail

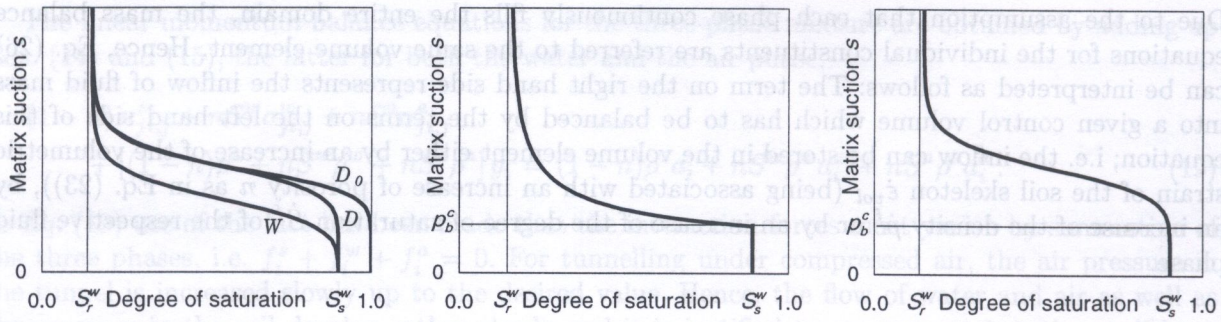

Fig. 4. (a) Experimentally determined relationship between S^w and s and approximations according to (b) Brooks and Corey [5] and (c) van Genuchten [6]

in [5] and is used in the approach presented in [14]. An improved approximation proposed by van Genuchten [6] is depicted in Fig. 4c. For stresses in the air phase different from the atmospheric pressure the matrix suction s has to be replaced by the capillary stress p^c according to Eq. (7).

The approximation of relation (29) proposed by Brooks and Corey is given as

$$S^w = S_r^w + (S_s^w - S_r^w) \left(\frac{p_b^c}{p^c} \right)^{\lambda} \tag{30}$$

and the one developed by van Genuchten as

$$S^w = S_r^w + (S_s^w - S_r^w) \left[1 + \left(\frac{p^c}{p_b^c} \right)^n \right]^{-m} . \tag{31}$$

In Eqs. (30) and (31) p_b^c denotes the air entry value (bubbling pressure) which can be viewed as a characteristic pressure that has to be reached before the air actually enters the pores. λ, m and n are empirical constants to fit the curves to experimental data. Mualem determined these parameters for a large number of soils which in extracts are given in [16]. In the present model the approximation of the relationship between S^w and p^c by van Genuchten is used.

3. Weak formulation of the basic equations

For the numerical solution of problems involving a three-phase medium weak formulations of the equilibrium equations for the three-phase mixture (20) and of the mass balance equations for the different constituents (26) are required.

Using the principle of virtual displacements and taking into account the partitioning of the total stress tensor as described in Eq. (6), the weak formulation of the equilibrium equations for quasi-static conditions (20) is obtained as

$$- \int_V \tilde{\sigma}'_{ij} \, \delta\varepsilon_{ij} \, \mathrm{d}V - \int_V S^w \, p^w \, \delta_{ij} \, \delta\varepsilon_{ij} \, \mathrm{d}V - \int_V S^a \, p^a \, \delta_{ij} \, \delta\varepsilon_{ij} \, \mathrm{d}V$$

$$+ \int_V \tilde{\rho} g_i \, \delta u_i \, \mathrm{d}V + \int_S \tilde{t}_i \, \delta u_i \, \mathrm{d}S = 0 , \tag{32}$$

where δu_i and $\delta\varepsilon_{ij}$ denote virtual displacements and virtual strains, respectively, and δ_{ij} is the Kronecker-Delta. V and S are the volume and the surface of the domain under consideration.

Dividing Eq. (26) by ρ^f, substituting Darcy's law (17) and the constitutive relationship for the fluid phase f (28) into this equation, multiplying the resulting equation by a virtual hydrostatic stress δp^f, integrating over the domain under consideration and applying the divergence theorem to

the term containing the divergence of $\tilde{\mathbf{v}}^{fr}$ yields the following weak formulation of the mass balance equation for the fluid phase f:

$$\int_V \delta p^f \left\{ S^f \dot{\varepsilon}_{vol} - \frac{nS^f}{K^f}\dot{p}^f + n\dot{S}^f \right\} \mathrm{d}V - \int_V \delta p^f_{,i} \frac{k^f}{\gamma^f} \left(p^f_{,i} + \rho^f g_i \right) \mathrm{d}V + \int_S \delta p^f \, \tilde{q}^f \, \mathrm{d}S = 0 \tag{33}$$

with $\tilde{q}^f$ denoting the averaged flux of the respective fluid phase through the boundary $\mathrm{d}S$ of the particular domain.

4. Numerical implementation into a finite element programme

Spatial discretization of Eqs. (32) and (33), the latter for both the water phase with $f = w$ and the air phase with $f = a$, respectively, within the framework of the finite element method (FEM) involves subdivision of the domain V under consideration into finite elements. The displacements of the soil skeleton $\mathbf{u}$ and the hydrostatic stresses in the water and the air phase, p^w and p^a, are chosen as primary variables. Within a single finite element e they are approximated in terms of a matrix of suitable shape functions $\mathbf{N}_u$ and of a vector of suitable shape functions $\mathbf{N}_p$ and of the respective vectors of the nodal values of the displacements, $\mathbf{U}_e$, and of the hydrostatic fluid stresses, $\mathbf{P}^w_e$ and $\mathbf{P}^a_e$, as

$$\mathbf{u}_e = \mathbf{N}_u \, \mathbf{U}_e \,, \qquad p^w_e = (\mathbf{N}_p)^T \, \mathbf{P}^w_e \,, \qquad p^a_e = (\mathbf{N}_p)^T \, \mathbf{P}^a_e \,. \tag{34}$$

Usually, different orders of interpolation are chosen for the different variables, e.g., for plane strain and axisymmetric problems the displacements are interpolated with quadratic polynomials $\mathbf{N}_u$ and the hydrostatic stresses with bilinear polynomials $\mathbf{N}_p$.

Assuming first the discretization to consist only of a single finite element, substitution of the approximations for the primary variables (34) into the weak formulation of the equilibrium equations for the three-phase mixture (32) yields

$$\begin{aligned} &-(\delta \mathbf{U}_e)^T \int_{V_e} \mathbf{B}_u^T \, \tilde{\boldsymbol{\sigma}}' \, \mathrm{d}V_e - (\delta \mathbf{U}_e)^T \int_{V_e} \mathbf{B}_u^T \, \mathbf{1} S^w \, \mathbf{N}_p^T \, \mathrm{d}V_e \, \mathbf{P}^w_e - (\delta \mathbf{U}_e)^T \int_{V_e} \mathbf{B}_u^T \, \mathbf{1} S^a \, \mathbf{N}_p^T \, \mathrm{d}V_e \, \mathbf{P}^a_e \\ &+ (\delta \mathbf{U}_e)^T \int_{V_e} \mathbf{N}_u^T \, \tilde{\mathbf{b}} \, \mathrm{d}V_e + (\delta \mathbf{U}_e)^T \int_{S_e} \mathbf{N}_u^T \, \tilde{\mathbf{t}} \, \mathrm{d}S_e = \mathbf{0} \,. \end{aligned} \tag{35}$$

In Eq. (35) $\mathbf{B}_u$ contains the derivatives of the shape functions $\mathbf{N}_u$ with respect to the coordinates, $\mathbf{1}$ is a vector comparable to the Kronecker-Delta, $\tilde{\mathbf{b}} = \tilde{\rho}\mathbf{g}$ is the vector of the body forces and $\tilde{\mathbf{t}}$ denotes the surface tractions; V_e is the volume and S_e the surface of the finite element e. The discretization of the weak formulation of the mass balance equation for a fluid phase f (33) can be derived in a similar manner,

$$\begin{aligned} &\left(\delta \mathbf{P}^f_e\right)^T \int_{V_e} \mathbf{N}_p \, S^f \mathbf{1}^T \, \mathbf{B}_u \, \mathrm{d}V_e \, \dot{\mathbf{U}}_e - \left(\delta \mathbf{P}^f_e\right)^T \int_{V_e} \mathbf{N}_p \frac{nS^f}{K^f} \mathbf{N}_p^T \, \mathrm{d}V_e \, \dot{\mathbf{P}}^f_e \\ &+ \left(\delta \mathbf{P}^f_e\right)^T \int_{V_e} \mathbf{N}_p \, n \frac{\mathrm{d}S^f}{\mathrm{d}p^c} \mathbf{N}_p^T \, \mathrm{d}V_e \left(\dot{\mathbf{P}}^a_e - \dot{\mathbf{P}}^w_e \right) - \left(\delta \mathbf{P}^f_e\right)^T \int_{V_e} \mathbf{B}_p \, \frac{k^f}{\gamma^f} \left[\mathbf{B}_p^T \, \mathbf{P}^f_e + \rho^f \mathbf{g} \right] \mathrm{d}V_e \\ &+ \left(\delta \mathbf{P}^f_e\right)^T \int_{S_e} \mathbf{N}_p \, \tilde{q}^f \, \mathrm{d}S_e = 0 \,, \end{aligned} \tag{36}$$

with $\mathbf{B}_p$ containing the derivatives of the shape functions $\mathbf{N}_p$.

Extending the discretization in Eqs. (35) and (36) to a domain with an arbitrary number of finite elements, making use of the fact that the resulting equations hold for arbitrary virtual displacements

$\delta\mathbf{U}$ and virtual hydrostatic stresses $\delta\mathbf{P}^f$ and assembling the vectors and matrices for the individual elements according to standard procedures yields the coupled system of equations

$$\begin{aligned} \mathbf{f}^{in} + \mathbf{C}^w\,\mathbf{P}^w + \mathbf{C}^a\,\mathbf{P}^a &= \mathbf{f}^{ex}\,, \\ (\mathbf{C}^w)^T\,\dot{\mathbf{U}} - \mathbf{S}^w\,\dot{\mathbf{P}}^w + \mathbf{C}^{wa}\,\dot{\mathbf{P}}^a - \mathbf{H}^w\,\mathbf{P}^w &= \dot{\mathbf{f}}^w\,, \\ (\mathbf{C}^a)^T\,\dot{\mathbf{U}} - \mathbf{S}^a\,\dot{\mathbf{P}}^a + \mathbf{C}^{wa}\,\dot{\mathbf{P}}^w - \mathbf{H}^a\,\mathbf{P}^a &= \dot{\mathbf{f}}^a\,. \end{aligned} \tag{37}$$

In Eq. (37) $\mathbf{U}$, $\mathbf{P}^w$ and $\mathbf{P}^a$ denote the global vectors of the nodal values for the displacements of the soil skeleton and for the hydrostatic stresses in the fluid phases water and air; $\mathbf{f}^{in}$ and $\mathbf{f}^{ex}$ are the vectors of the internal forces of the soil skeleton and the external forces, respectively; the matrices $\mathbf{C}^w$, $\mathbf{C}^a$ and $\mathbf{C}^{wa}$ describe the coupling between the individual constituents, i.e. between the water phase and the soil skeleton, between the air phase and the soil skeleton and between the two fluid phases, respectively; $\mathbf{S}^w$ and $\mathbf{S}^a$ contain the compressibility of the particular fluid and the constitutive relationship between the degree of water saturation and the capillary stress; $\mathbf{H}^w$ and $\mathbf{H}^a$ are the permeability matrices and the vectors $\dot{\mathbf{f}}^w$ and $\dot{\mathbf{f}}^a$ are associated with the flow of the respective fluid due to gravity and the flow through the surface of the domain under consideration.

$\dot{\mathbf{U}}$, $\dot{\mathbf{P}}^w$ and $\dot{\mathbf{P}}^a$ denote time derivatives of the vectors of nodal values. Therefore, a numerical integration in the time domain has to be performed. Assuming the solution to be known for the discrete point of time t_n and Δt_{n+1} being the current time step size, application of the implicit and unconditionally stable Euler backward integration scheme results in

$$\mathbf{X}_{n+1} = \mathbf{X}_n + \dot{\mathbf{X}}_{n+1}\Delta t_{n+1} \qquad \text{with} \qquad \mathbf{X} = \lfloor\, \mathbf{U}\ \ \mathbf{P}^w\ \ \mathbf{P}^a \,\rfloor^T\,, \tag{38}$$

where $\mathbf{X}_n$ and $\mathbf{X}_{n+1}$ denote the known and unknown solution for the nodal values at the discrete points of time t_n and t_{n+1}, respectively. Making use of Eq. (38) in (37) yields the following coupled set of equations for the incremental nodal values:

$$\begin{bmatrix} \mathbf{K} & \mathbf{C}^w_{n+1} & \mathbf{C}^a_{n+1} \\ (\mathbf{C}^w_{n+1})^T & -\mathbf{S}^w_{n+1} - \Delta t_{n+1}\,\mathbf{H}^w_{n+1} & \mathbf{C}^{wa}_{n+1} \\ (\mathbf{C}^a_{n+1})^T & \mathbf{C}^{wa}_{n+1} & -\mathbf{S}^a_{n+1} - \Delta t_{n+1}\,\mathbf{H}^a_{n+1} \end{bmatrix} \begin{Bmatrix} \Delta\mathbf{U}_{n+1} \\ \Delta\mathbf{P}^w_{n+1} \\ \Delta\mathbf{P}^a_{n+1} \end{Bmatrix}$$

$$= \begin{Bmatrix} \mathbf{f}^{ex}_{n+1} - \mathbf{f}^{in}_n - \mathbf{C}^w_{n+1}\mathbf{P}^w_n - \mathbf{C}^a_{n+1}\mathbf{P}^a_n \\ \Delta t_{n+1}(\dot{\mathbf{f}}^w_{n+1} + \mathbf{H}^w_{n+1}\mathbf{P}^w_n) \\ \Delta t_{n+1}(\dot{\mathbf{f}}^a_{n+1} + \mathbf{H}^a_{n+1}\mathbf{P}^a_n) \end{Bmatrix}. \tag{39}$$

In Eq. (37) the partitioning of the vector of the internal forces valid for linear elastic behaviour of the soil skeleton, $\mathbf{f}^{in}_{n+1} = \mathbf{f}^{in}_n + \Delta\mathbf{f}^{in}_{n+1}$, with $\Delta\mathbf{f}^{in}_{n+1} = \mathbf{K}\,\Delta\mathbf{U}_{n+1}$ and $\mathbf{K}$ representing the stiffness matrix of the soil skeleton, was used to arrive at Eq. (39). Although Eq. (39) refers to the special case of linear elastic constitutive behaviour of the soil skeleton the equation is still non-linear. This follows from the dependence of the matrices $\mathbf{C}$, $\mathbf{S}$ and $\mathbf{H}$ and of the vectors $\dot{\mathbf{f}}$ on the nodal values of the fluid pressures because $\mathbf{C}$, $\mathbf{S}$, $\mathbf{H}$ and $\dot{\mathbf{f}}$ are functions of either the degree of saturation (29) or the permeability coefficients (18). Hence, the system of equations has to be solved iteratively for each time step, e.g., by means of a direct iteration procedure. Contrary to the approach presented in [14], it follows from Eq. (39) that the system of coupled equations is solved for the incremental values of the unknowns and not for the total values.

5. Validation of the numerical model

The complex implementation procedure of the three-phase soil model into the FE programme AFENA [4] was subdivided into several steps. For the verification of the FE code and for the

validation of the mechanical model a number of experiments either reported in the literature or conducted to this end were simulated numerically.

As an example for verifying the two-phase formulation for completely saturated conditions an experiment conducted at the Institute for Soil Mechanics and Foundation Engineering at the Technical University of Graz within the framework of the *Austrian Joint Research Initiative* on *Numerical Simulation in Tunnelling* [1] is employed. It deals with the flow of compressed air through dry soil [10]. Hence, it can be viewed as a consolidation problem, however, taking into account the compressibility of the fluid phase.

The two-phase formulation for unsaturated conditions is checked by simulating a laboratory test performed by Liakopoulos [15] dealing with dewatering of a column of sand due to gravity only. It is well-documented in the literature [14] and has been used by a number of research groups to check their numerical models [9].

For the verification of the complete three-phase formulation the latter experiment is employed again, allowing the air pressure to differ from the atmospheric one. However, in contrast to the results presented in the literature [14], the time period of the numerical simulation is extended until all quantities attain a steady state.

In addition to the academic examples mentioned up to now a large-scale in-situ air permeability test [13] carried out in connection with the application of compressed air at the subway construction site in Essen, Germany, is simulated numerically. In this experiment compressed air is employed for dewatering the soil and thus the test has practical relevance for pneumatic tunnelling below the ground-water level.

5.1. Flow of compressed air through dry soil

In the experiments conducted at the Institute for Soil Mechanics and Foundation Engineering at the Technical University of Graz the air loss through cracks in the shotcrete lining and the flow of compressed air in the adjacent soil are investigated for different types of soil and various degrees of water saturation. In the test considered here a steel container filled with *dry* sand is placed on top of a shotcrete element containing a crack of defined width (Fig. 5a). Young's modulus and Poisson's ratio of the soil are given as $E = 24\ 048.0$ kPa and $\nu = 0.23$, respectively. The permeability of the soil with respect to the water phase is determined for fully saturated conditions as $k^{ow} = 2.0{-}3.0{\cdot}10^{-5}$ m/s. The porosity is found to be $n = 0.37$. The densities for both constituents

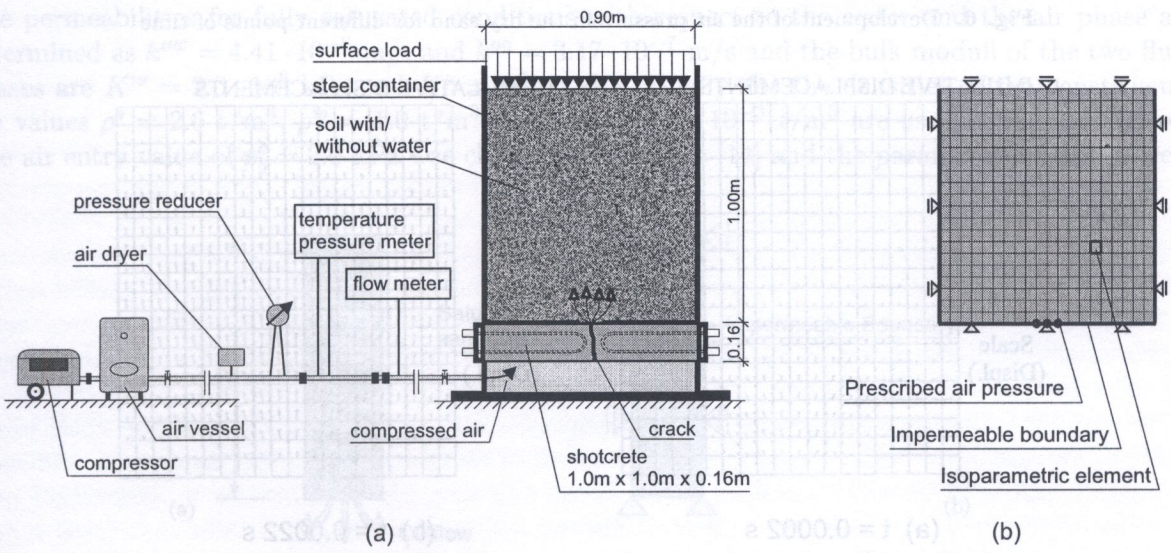

Fig. 5. (a) Set-up of the laboratory tests, conducted at the TU-Graz [10] and (b) FE model

are determined as $\rho^s = 2.62$ t/m^3 and $\rho^a = 1.295 \cdot 10^{-3}$ t/m^3, respectively. The bulk modulus of the air phase is assumed as $K^a = 100.0$ kPa.

In the experiment the overburden above the crown of the tunnel is simulated by a constant surface load of 250 kPa applied on top of the soil (Fig. 5a) using a grid system of girders and beams which is vertically prestressed and fixed by four spindle rods. At the bottom of the shotcrete slab an excess air pressure is applied causing compressed air to flow through the crack as well as through the adjacent dry sand. In the experiment the development of the air pressure in the soil is measured at selected points.

Figure 5b shows the finite element mesh together with both solid and fluid (only one fluid phase, i.e. compressed air) boundary conditions used in the analysis. The domain is fully constrained at the bottom, horizontally constrained at the vertical boundaries and vertically constrained at the top. The vertical and the bottom boundaries are assumed to be impermeable for the fluid phase, atmospheric air pressure prevails along the upper boundary. It should be mentioned that the overburden load of the soil specimen is accounted for in the geostatic stress conditions. The excess air pressure is applied at the bottom boundary of the soil column and amounts to 8.5 kPa (= 85 mbar). Thus, this excess air pressure represents a prescribed boundary condition for the fluid phase compressed air which is constant throughout the analysis. The adjustment of the air pressure in the soil specimen to this prescribed boundary condition is investigated in the numerical simulation.

Figure 6 shows the computed transient air pressure in the soil. Immediately after the application of the excess air pressure there is still atmospheric pressure in almost the entire soil specimen

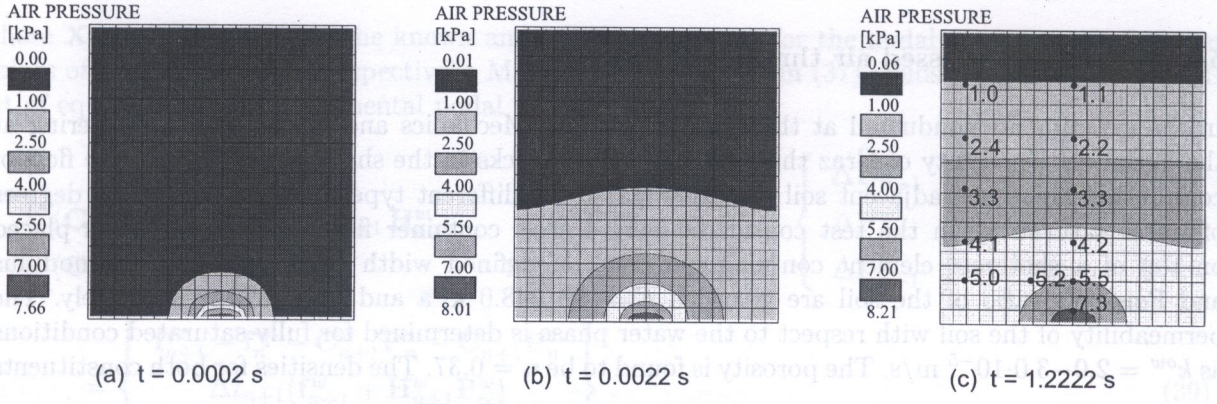

Fig. 6. Development of the air pressure in the dry sand for different points of time

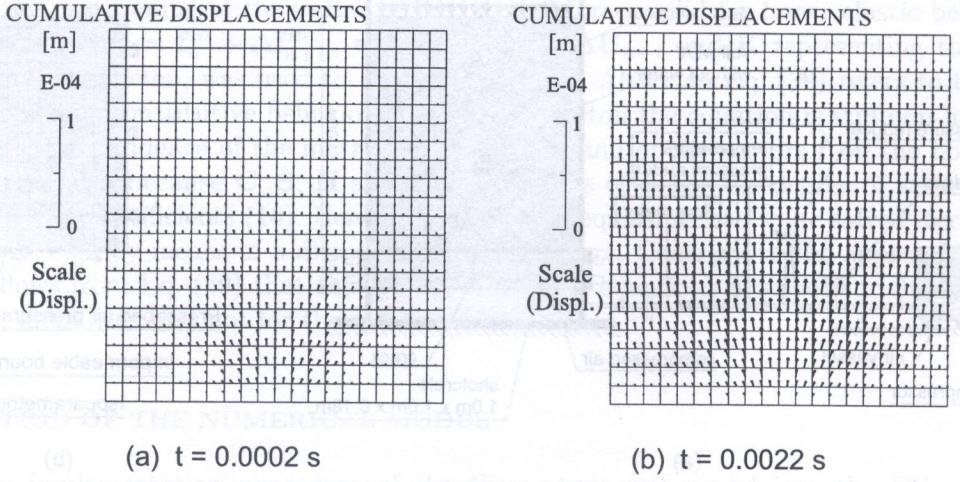

Fig. 7. Transient displacements of the soil skeleton

(Fig. 6a). Apart from the injection region, for each of the individual instants of time shown in Figs. 6a–c the distribution of the air pressure at a fixed height is quite uniform. Figure 6c shows the computed pressure distribution in the soil after steady state conditions have been attained. For the comparison of the numerical and the experimental results the measured values of the air pressure (dots and printed values) are included in this figure. It should be emphasized again that for the numerical simulation of this test a two-phase formulation is sufficient, i.e. only the solid and the air phase are necessary. However, in order to compute the time-dependent development of the air pressure in the soil the compressibility of the air has to be taken into account.

In addition to the development of the air pressure the transient displacements within the soil are computed. As one would expect the flow of air through the soil causes upwardly directed displacements of the soil skeleton which are shown in Fig. 7 for two discrete points of time (corresponding to the first two instants of time in Fig. 6). Due to the constraint applied at the top of the soil column the maximum values of the displacements at steady state conditions are obtained about half-way between the top and bottom boundaries.

For further details concerning the experiment and the numerical simulation the interested reader is referred to [8, 10], respectively.

5.2. Dewatering of a sand column under atmospheric conditions

This section is concerned with a benchmark test according to an experiment performed by Liakopoulos [15]. A principle sketch of the experiment is shown in Fig. 8a.

The problem deals with the dewatering of a column of Del Monte sand of 1 m height under atmospheric conditions, i.e. the dewatering process is driven by gravity only. Prior to the start of the experiment steady state conditions are prevailing in the sense that water is continuously added at the top and freely drains through a filter at the bottom of the column. At the onset of the test the water supply is stopped and the tensiometer readings to measure the tensile stresses in the water phase are recorded.

In an independent set of laboratory tests Liakopoulos determined the porosity and the hydraulic properties of the material; however, no mechanical parameters are reported for the soil. The experiment has been used as a benchmark test [9] by other research groups to check their numerical models. Thus, in order to be able to compare the current solution with results presented in the literature [14] the input data are chosen according to [14]. Young's modulus and Poisson's ratio are given as $E = 1300.0$ kPa and $\nu = 0.4$, respectively. The porosity of the sand amounts to $n = 0.2975$. The permeabilities for fully saturated conditions with respect to the water and the air phase are determined as $k^{ow} = 4.41 \cdot 10^{-6}$ m/s and $k^{oa} = 3.17 \cdot 10^{-7}$ m/s and the bulk moduli of the two fluid phases are $K^w = 2.0 \cdot 10^6$ kPa and $K^a = 100.0$ kPa. Finally, for the densities of the constituents the values $\rho^s = 2.0$ t/m^3, $\rho^w = 1.0$ t/m^3 and $\rho^a = 1.295 \cdot 10^{-3}$ t/m^3 are used in the calculation. The air entry value of $p_b^c = 2.0$ kPa was chosen according to [14] and the parameters m and n were

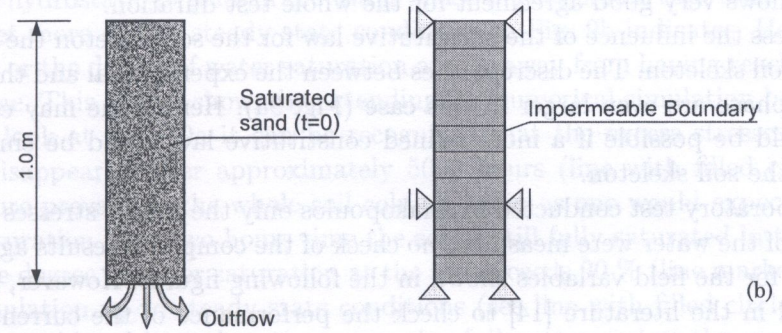

Fig. 8. Liakopoulos' experiment [15]: (a) Principle sketch and (b) FE model

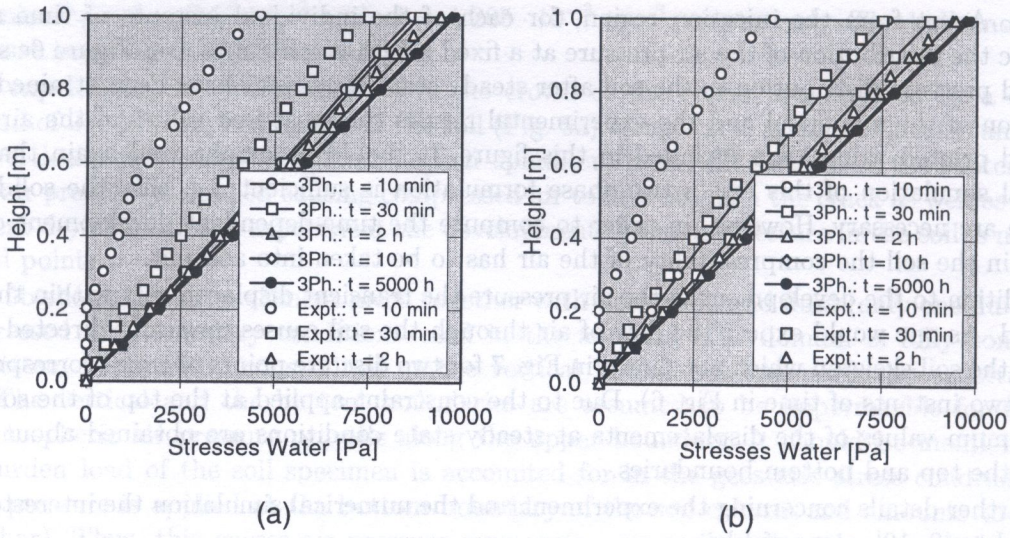

Fig. 9. Stresses in the water phase (a) for a rigid and (b) for an elastic soil skeleton

determined to fit the relationship between the capillary stress and the degree of water saturation to the empirical equation given in [14].

Figure 8b depicts the finite element model used in the analysis. The domain is discretized by ten isoparametric elements with quadratic interpolation for the displacement degrees of freedom and bilinear interpolation for the hydrostatic stresses in the fluid phases. The boundary conditions are specified as follows: The column is fully constrained at the bottom and horizontally constrained at the vertical boundaries; for the fluid phases water and air impervious vertical boundaries and atmospheric conditions together with free drainage at the top and at the bottom of the column are assumed. Since only the excess fluid stresses with respect to the atmospheric pressure are of interest, the actual value of the atmospheric pressure may be ignored (it cancels out in Eq. (7)). Hence, in the numerical results only excess stresses with respect to the atmospheric pressure are considered.

Figure 9 shows the transient stresses in the water phase versus the height of the sand column both for a rigid and an elastic soil skeleton. For the numerical results lines marked with different labels are used to refer to different points of time while for the experimental data the respective symbols without lines are employed.

Taking a look at the results with the elastic soil skeleton (Fig. 9b), quite substantial differences between the calculated and the measured data at the beginning of the test are recognized when comparing for example the graphs with the non-filled circles which refer to a point of time of ten minutes after the start of the experiment. At the final stage of the test after two hours time (lines with triangles) the numerical solution and the experimental data are almost identical. Contrary to the discrepancies between measured and computed results in the early test phase a comparison of the numerical results for the linear elastic soil skeleton (Fig. 9b) with the numerical solution reported in [14] shows very good agreement for the whole test duration.

In order to assess the influence of the constitutive law for the soil skeleton the problem was rerun assuming a rigid soil skeleton. The discrepancies between the experimental and the numerical results in the early test phase are even larger in this case (Fig. 9a). Hence, one may conclude that some improvement would be possible if a more refined constitutive law would be employed to describe the behaviour of the soil skeleton.

Since in the laboratory test conducted by Liakopoulos only the tensile stresses in the water phase and the flow rate of the water were measured, no check of the computed results against experimental data was possible for the field variables shown in the following figures. However, a comparison with solutions reported in the literature [14] to check the performance of the current numerical model showed good agreement. Moreover, some interesting conclusions can be drawn from the various pictures.

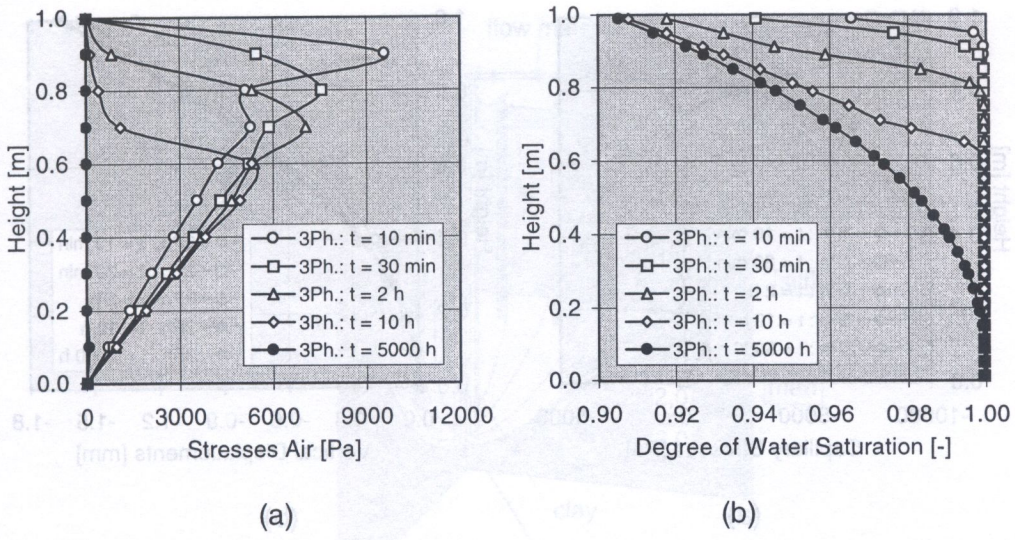

Fig. 10. (a) Stresses in the air phase and (b) degree of water saturation

Figure 10a shows the development of the hydrostatic stresses in the air phase versus height of the soil column for the case of an elastic soil skeleton. It should be noted that only the excess stresses in the air phase with respect to the atmospheric pressure are plotted in this figure. These excess stresses are tensile stresses. As can be seen, there is a clear peak of the excess air stress at about that level of the column where the degree of water saturation of the mixture starts decreasing below fully saturated conditions (de-wetting front). Just below this peak oscillations of the air stresses can be recognised. In order to avoid these oscillations, in [14] a lower limit of the relative air permeability was introduced. The transition from the fully saturated to the partially saturated state is treated numerically by introducing a very small but finite degree of air saturation in the water saturated part of the soil column. This is the reason why air stresses are also present in the lower fully saturated part of the soil column.

Figure 10b shows the de-wetting front moving down the sand column with increasing time, i.e. the degree of water saturation of the soil decreases below a fully saturated state starting at the top of the column and moving down as time goes on. The different lines indicate the position of the de-wetting front at different points of time, e.g. two hours after the start of the test the lower 80 cm of the column are still fully saturated (line with triangles). Moving down the column together with this de-wetting front is the peak in the excess hydrostatic air stresses as Fig. 10a shows very clearly. Since the degree of water saturation decreases starting from the top of the column, air is allowed to enter the pores of the soil resulting in an increase of the air pressure to the atmospheric pressure.

Calculations with a rigid soil skeleton yield quite similar curves, only the hydrostatic air stresses differ somewhat more in the very early test phase (first five minutes) which is reflected in a larger peak than the one for the elastic soil skeleton shown in Fig. 10a.

Considering the hydrostatic stresses in the water phase the two hours time span of the experiment was sufficient to get more or less steady state conditions as Fig. 9b indicates. However, quantities like the air stresses or the degree of water saturation are far away from having reached a steady state at that point of time. This can be shown by extending the numerical simulation beyond that period of time. Taking a look at Fig. 10a it can be recognized that the excess stresses in the air phase have completely disappeared after approximately 5000 hours (line with filled circles), i.e. finally atmospheric pressure prevails in the whole soil column again as one would expect. Concerning the degree of water saturation after two hours time the soil is still fully saturated in the lower 80 cm of the column and the degree of water saturation at the top exceeds 90 % (line marked with triangles). The numerical simulation up to steady state conditions (see line with filled circles) shows that for the particular soil considered here the column remains fully saturated at the very bottom and the degree of water saturation does not fall below 90 % at the top.

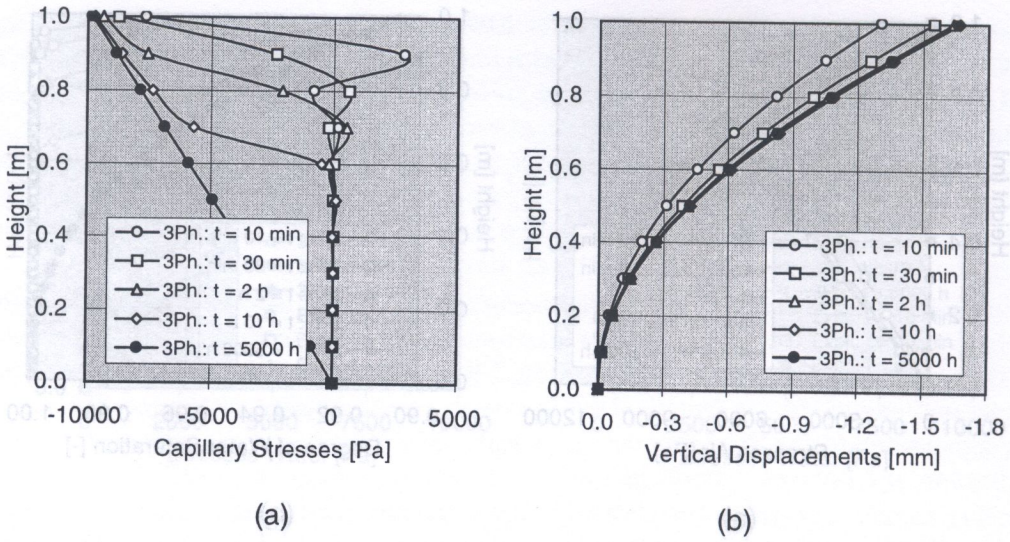

Fig. 11. (a) Capillary stresses and (b) vertical displacements of the soil skeleton

In Fig. 11a the development of the capillary stress versus the height of the soil column is shown for the case of an elastic soil skeleton. Since, according to Eq. (7), the capillary stress is defined as the difference between the hydrostatic stresses in the water and the air phase, this diagram follows straightforward from the previous Figs. 10a and 9b. The linear distribution of the capillary pressure along the height of the column at the finally attained steady state conditions is quite obvious considering the linear stress distribution in the water phase (line with filled circles in Fig. 9b) and the atmospheric pressure in the air phase (line with filled circles in Fig. 10a) at the final stage.

Figure 11b depicts the calculated vertical displacements of the soil versus the height of the sand column. As one would expect the soil is compacted by the dewatering process and the computation predicts a maximum settlement of about 1.65 mm at the top of the column.

The results discussed in this subsection generally show very good agreement compared with other numerical solutions presented in the literature [11, 14]. However, whereas most of these calculations are restricted to a time period of two hours according to Liakopoulos' experiment, here also the extended time span until attaining steady state conditions has been considered. The two main conclusions to be drawn from the numerical simulation beyond the time span of the experiment are that (i) finally atmospheric air pressure prevails in the whole soil column again and (ii) for the particular type of soil considered here it is not possible to completely dewater the specimen under the influence of gravitation only.

5.3. Dewatering of soil by means of compressed air

In connection with the application of compressed air for the subway construction in Essen, Germany, a full-scale in-situ air permeability test was carried out [13]. The primary aims of this project focussed on the investigation of (i) the air permeability of the Essen soil, i.e. on the determination of the air permeability coefficients of the various soil layers and their time- and pressure-dependent changes, (ii) the extent of the air flow field and (iii) the influence of the flow of compressed air on the deformations of the soil skeleton.

Figure 12 contains a sketch of the experimental set-up. In total three different sets of tests were performed where compressed air was injected into the ground via a large bore hole (1.5 m diameter) at different depths below the ground surface according to the various types of outcropping soil. In test 1A compressed air was pumped into the ground at a depth where rather weathered marl was encountered and thus the joints were less pronounced while in test 1B undisturbed and jointed marl appeared at the air injection level. In experiment 2 compressed air was injected in the transition

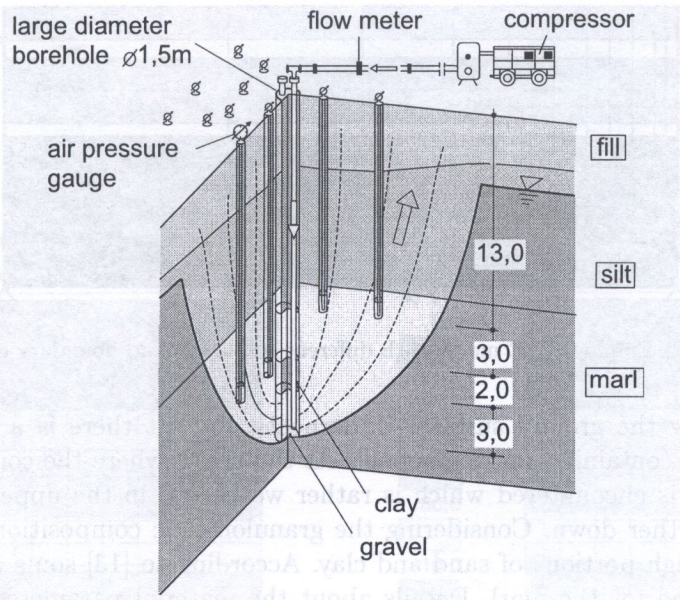

Fig. 12. Set-up of the in-situ air permeability test in Essen (dimensions in [m])

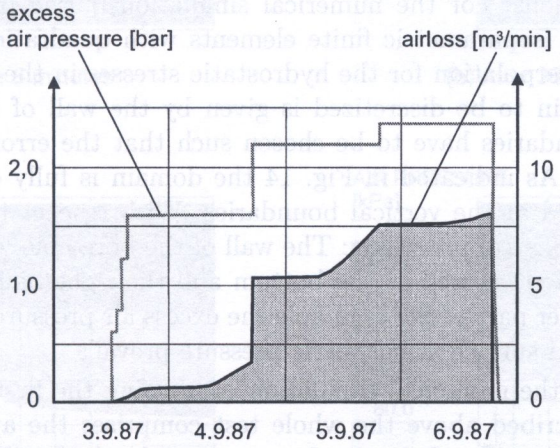

Fig. 13. Different excess air pressure levels versus time (date)

zone between marl and silt and the soil additionally was grouted. In a number of smaller bore holes located in the vicinity of the main one the air pressure in the soil was measured at different distances from the point of air injection and at various depths below the ground surface.

In experiment 1B which is considered here compressed air was injected into the ground between a depth of 18 and 21 m below the ground surface with an excess air pressure up to 2.35 bar. It was applied in three steps (1.60, 2.20 and 2.35 bar) keeping the pressure constant for about one day at each of the three levels. Figure 13 shows the three air pressure levels and the air loss versus time. It follows from Fig. 13 that at each pressure level the air loss increased after some time. This can be attributed to the increasing air permeability of the soil which is associated with the reduction of the degree of water saturation due to the displacement of the ground-water by the compressed air.

From the documentation of this experiment in the literature [13] it follows that, in contrast to the sketch in Fig. 12, the soil profile at the test location actually consists of four distinct layers (Fig. 14). At the top a fill layer of about 3 m thickness is encountered mainly composed of sand and silt but also containing parts of construction debris. Following is a 7 to 8 m thick silt layer with portions of sand in the upper- and organic additions in the lower parts. Its permeability both with respect to water and air is rather low. In this layer also the ground-water table is located at a depth

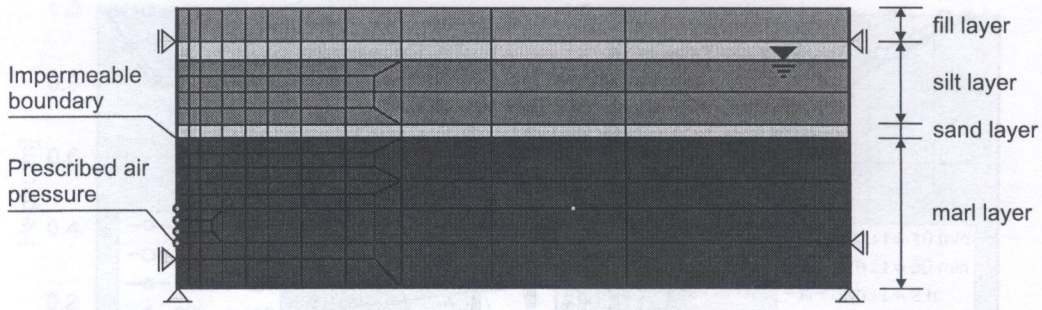

Fig. 14. Employed FE model with different soil layers and boundary conditions

of about 4.7 m below the ground surface. Underneath the silt there is a thin highly permeable sand-gravel layer also containing portions of silt. At the depth where the compressed air is injected a thick layer of marl is encountered which is rather weathered in the upper region while showing pronounced joints further down. Considering the granulometric composition the marl corresponds to a silt containing high portions of sand and clay. According to [13] some averaged values for the permeabilities are used for the marl. Details about the material parameters of the various layers can also be found in [13].

The discretization of the above described soil profile is shown in Fig. 14 together with the appropriate boundary conditions. For the numerical simulation of the problem advantage of axial symmetry has been taken. Isoparametric finite elements with quadratic interpolation for the displacements and bilinear interpolation for the hydrostatic stresses in the fluid phases are used. The left boundary of the domain to be discretized is given by the wall of the bore hole whereas the right and the bottom boundaries have to be chosen such that the error induced by this artificial boundaries remains small. As indicated in Fig. 14 the domain is fully constrained at the bottom and horizontally constrained at the vertical boundaries. With respect to the two fluid phases the following boundary conditions are prevailing: The wall of the bore hole, except the filter part where the compressed air is injected, as well as the bottom and the right boundaries are assumed to be impermeable. Along the filter part of the bore hole the excess air pressure applied in the experiment is prescribed. At the ground surface atmospheric pressure prevails.

Finally, some results of the numerical simulation concerning the first pressure level of the field test are presented. As described above the whole test comprises the application of an excess air pressure of 2.35 bar in three steps. Only the first pressure level of 1.60 bar is considered here. It should be mentioned that in all the following plots only a sector of the discretized domain in the vicinity of the bore hole is shown.

Figure 15 shows the computed distributions of the air pressure in the soil at four different instants of time after the air pressure of 1.60 bar has been applied in the bore hole. Shortly after the start of the experiment only the region close to the filter part is affected by the applied air pressure as one would expect (Fig. 15a). With increasing time the influenced region becomes larger and larger. Finally, Fig. 15d refers to the air pressure distribution attained at the end of the first pressure level after approximately one day. In order to compare the numerical results with experimental data isolines composed from the recorded air pressure gauge values have been included in Fig. 15d. The calculations agree quite well with the measurements in the in-situ test as can be seen from this figure.

The development of the air pressure mainly takes place in the first phase after application of the pressure as Fig. 15 indicates. For the degree of water saturation, which is depicted for four different points of time in Fig. 16, on the other hand, after 4 hours only the region rather close to the air injection part of the bore hole shows a decrease from fully saturated conditions as can be seen from Fig. 16b. The soil above the ground-water level represented by the upper two rows of elements remains at the initial conditions – in the fill layer the degree of water saturation amounts to approximately 20 % and the linear decrease of the water saturation above the ground-water level represents the capillary fringe.

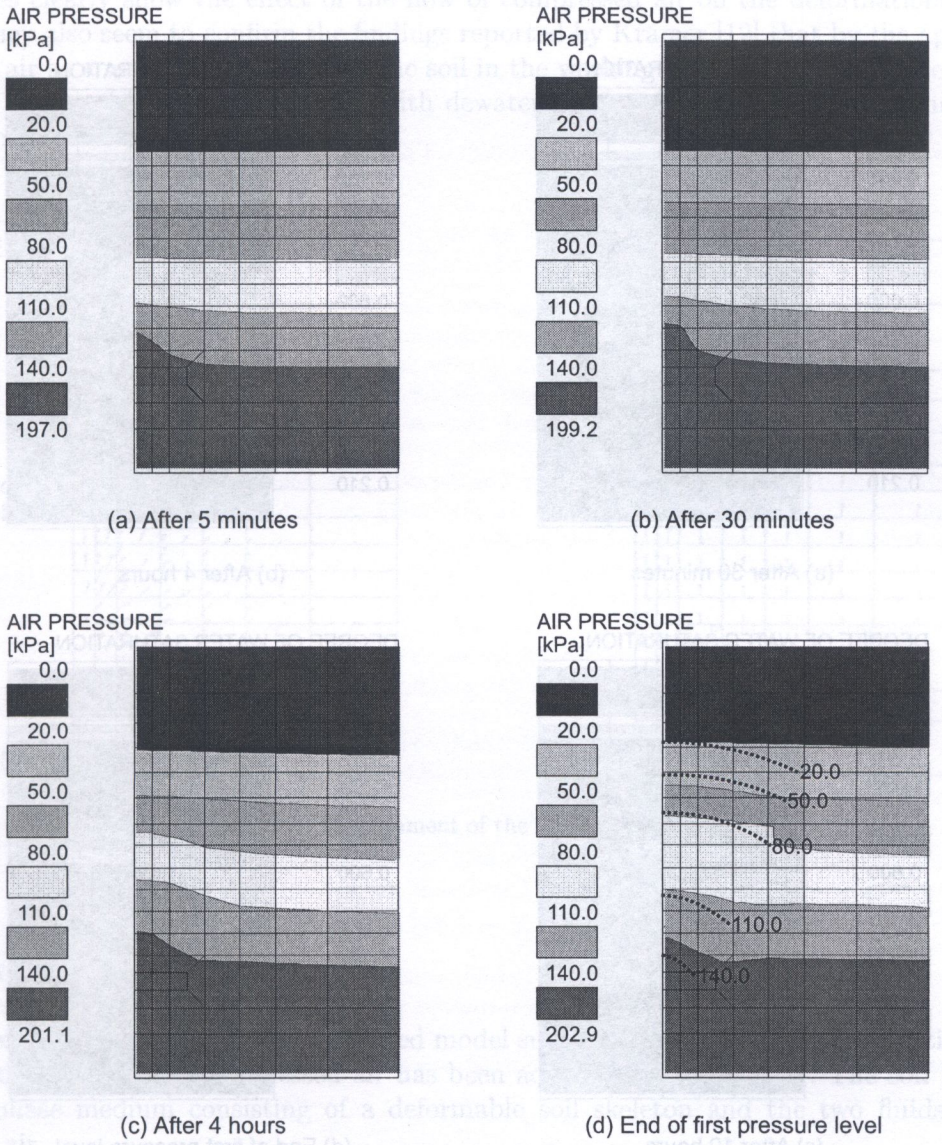

Fig. 15. Development of the excess air pressure [kPa] in the soil

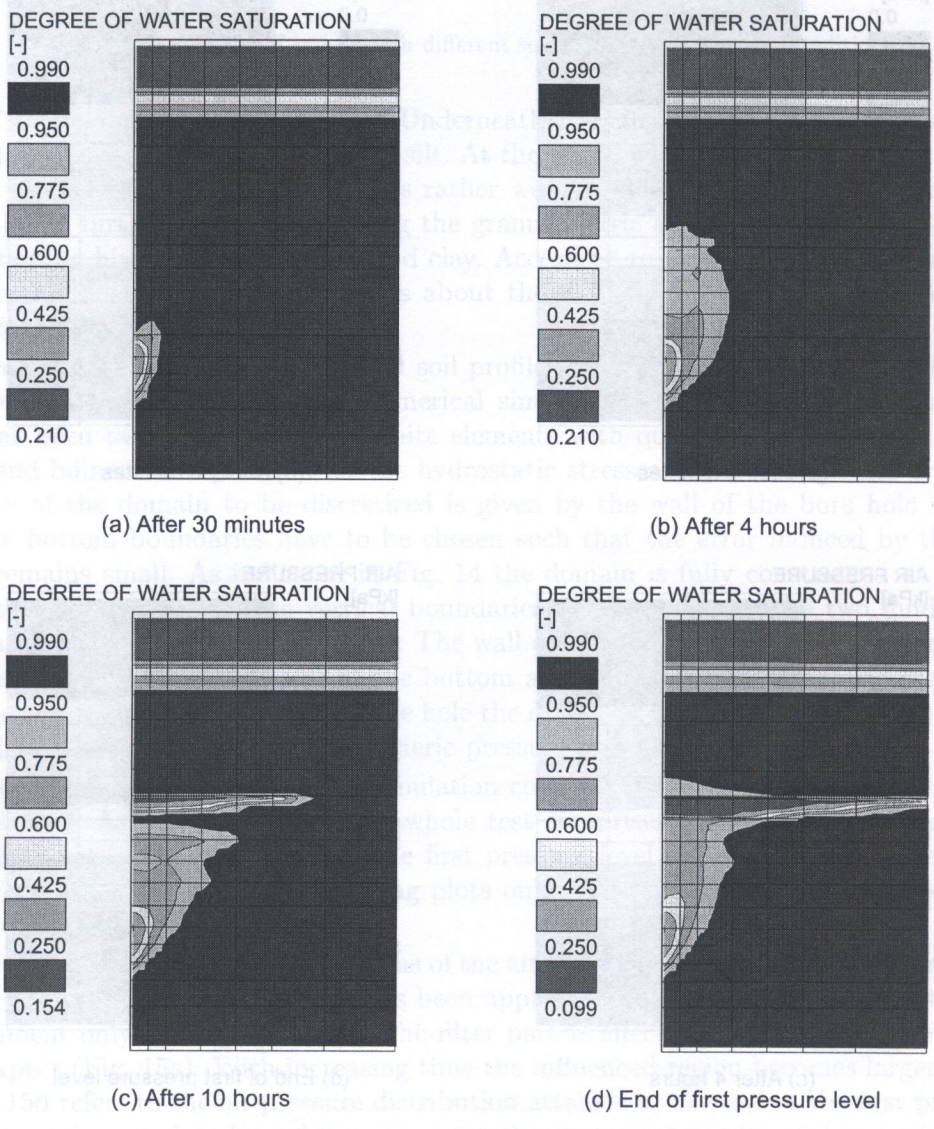

Fig. 16. Development of the degree of water saturation in the soil

At the end of the first pressure level after about one day (Fig. 16d) the thin highly permeable sand-gravel layer is almost completely dewatered. Emanating from the air injection part of the bore hole a cone is formed containing soil mass with a considerably lower degree of water saturation compared with the initial conditions. This cone also indicates the extent of the air flow field. Due to the highly permeable sand-gravel layer it is not possible to significantly dewater the soil above this layer by means of the currently applied pressure head of the first pressure level.

Figure 17 contains vector plots of the displacements of the soil skeleton for two points of time. These figures clearly show the effect of the flow of compressed air on the deformations of the soil skeleton. They also seem to confirm the findings reported by Kramer [12] that by the application of compressed air as a means for dewatering the soil in the working area of the tunnel face the ground settlements tend to be smaller compared with dewatering by pumping wells and tunnelling under atmospheric conditions.

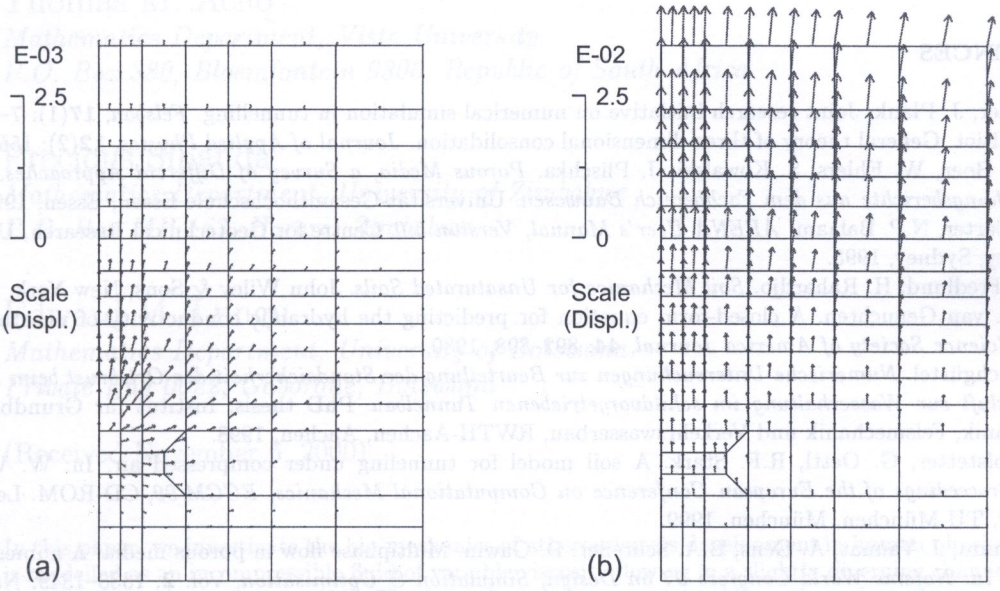

Fig. 17. Development of the soil displacements

6. Conclusions

The development and verification of a coupled model suitable for the numerical simulation of dewatering the soil by means of compressed air has been addressed in this paper. The soil is described as a three-phase medium consisting of a deformable soil skeleton and the two fluids water and compressed air.

In the first part of the paper the governing equations of the model and the numerical formulation within the framework of the finite element method have been presented. In the second part which is devoted to the verification of the developed FE code and the validation of the mechanical model three different example problems have been discussed.

Concluding from the numerical results the current model is able to describe a broad range of different phenomena encountered in geotechnical engineering. Starting with the well-known consolidation theory which is included as a special case also more sophisticated problems like dewatering under atmospheric conditions or dewatering by means of compressed air are covered by the approach. The numerical solutions presented show fairly good agreement with experimental data for all the examples, representing different degrees of complexity of the model. Of most practical relevance for further applications of the model to tunnelling under compressed air is of course the last

example dealing with the numerical simulation of a large-scale in-situ test of dewatering of soil by means of compressed air.

Although some of the parameters for the three-phase model, especially those for the constitutive relationship between the degree of water saturation and the capillary pressure, have to be estimated from data available in the literature the comparison of computed and measured results provides valuable insight into the potential of the model.

ACKNOWLEDGEMENT

The work described in this paper is part of a research project within the framework of the *Austrian Joint Research Initiative* on *Numerical Simulation in Tunnelling* which is funded by the Austrian Science Fund (FWF) under project number S08005-TEC. This support is gratefully acknowledged.

REFERENCES

[1] G. Beer, J. Plank. Joint research initiative on numerical simulation in tunnelling. *Felsbau*, **17**(1): 7–9, 1999.

[2] M.A. Biot. General theory of three-dimensional consolidation. *Journal of Applied Physics*, **12**(2): 155–164, 1941.

[3] R. de Boer, W. Ehlers, S. Kowalski, J. Plischka. *Porous Media, a Survey of Different Approaches*, Vol. **54** of *Forschungsberichte aus dem Fachbereich Bauwesen*. Universität-Gesamthochschule Essen, Essen, 1991.

[4] J.P. Carter, N.P. Balaam. *AFENA User's Manual, Version 5.0*. Centre for Geotechnical Research, University of Sydney, Sydney, 1995.

[5] D.G. Fredlund, H. Rahardjo. *Soil Mechanics for Unsaturated Soils*. John Wiley & Sons, New York, 1993.

[6] M.Th. van Genuchten. A closed-form equation for predicting the hydraulic conductivity of unsaturated soils. *Soil Science Society of America Journal*, **44**: 892–898, 1980.

[7] T. Hochgürtel. *Numerische Untersuchungen zur Beurteilung der Standsicherheit der Ortsbrust beim Einsatz von Druckluft zur Wasserhaltung im schildvorgetriebenen Tunnelbau*. PhD thesis, Institut für Grundbau, Bodenmechanik, Felsmechanik und Verkehrswasserbau, RWTH-Aachen, Aachen, 1998.

[8] G. Hofstetter, G. Oettl, R.F. Stark. A soil model for tunneling under compressed air. In: W. Wunderlich, ed., *Proceedings of the European Conference on Computational Mechanics, ECCM'99*, CD-ROM. Lehrstuhl für Statik, TU München, München, 1999.

[9] C. Jommi, J. Vaunat, A. Gens, B.A. Schrefler, D. Gawin. Multiphase flow in porous media: A numerical benchmark. In: *Nafems World Congress 97 on Design, Simulation & Optimisation*, Vol. **2**, 1338–1349. Nafems Ltd., Glasgow, 1997.

[10] G. Kammerer. *Experimentelle Untersuchungen von Strömungsvorgängen in teilgesättigten Böden und in Spritzbetonrissen im Hinblick auf den Einsatz von Druckluft zur Wasserhaltung im Tunnelbau*. PhD thesis, Institut für Bodenmechanik und Grundbau, Technische Universität Graz, Graz, 2000.

[11] G. Klubertanz. *Zur hydromechanischen Kopplung in dreiphasigen porösen Medien*. PhD thesis, École Polytechnique Fédérale de Lausanne, Lausanne, 1999.

[12] J. Kramer. U-Bahn Bau in Essen, Baulos 30 - Spritzbetonbauweise unter Druckluft: Luftverbrauch und Spannungsumlagerungen im Boden, Senkungen. In: *Proceedings der STUVA Tagung, Essen*, Vol. **32** of *Forschung + Praxis*, 193–199. STUVA, Essen, 1987.

[13] J. Kramer, S. Semprich. Erfahrungen über Druckluftverbrauch bei der Spritzbetonbauweise. *Taschenbuch für den Tunnelbau*, **13**: 91–153, 1989.

[14] R.W. Lewis, B.A. Schrefler. *The Finite Element Method in the Static and Dynamic Deformation and Consolidation of Porous Media*. John Wiley & Sons, Chichester, 2nd edition, 1998.

[15] A.C. Liakopoulos. *Transient Flow Through Unsaturated Porous Media*. PhD thesis, University of California, Berkeley, 1965.

[16] Y. Mualem. A new model for predicting the hydraulic conductivity of unsaturated porous media. *Water Resources Research*, **12**(3): 513–522, 1976.

[17] B.A. Schrefler, Z. Xiaoyong. A fully coupled model for water flow and airflow in deformable porous media. *Water Resources Research*, **29**(1): 155–167, 1993.

[18] O.C. Zienkiewicz, Y.M. Xie, B.A. Schrefler, A. Ledesma, N. Bićanić. Static and dynamic behaviour of soils: A rational approach to quantitative solutions. ii. semi-saturated problems. *Proceedings of the Royal Society of London*, **A**(429): 311–321, 1990.